Di et al. Nanoscale Research Letters (2018) 13:257
https://doi.org/10.1186/s11671-018-2671-6

Nanoscale Research Letters

NANO IDEA Open Access

Facile Synthesis and Enhanced Visible-Light Photocatalytic Activity of Novel p-Ag_3PO_4/n-$BiFeO_3$ Heterojunction Composites for Dye Degradation

Lijing Di[1,2], Hua Yang[1*], Tao Xian[2] and Xiujuan Chen[1]

Abstract

In this work, Ag_3PO_4 microparticles were decorated onto the surface of $BiFeO_3$ microcuboids through a precipitation method to obtain p-Ag_3PO_4/n-$BiFeO_3$ heterojunction composites. The composites were employed for the degradation of acid orange 7 (AO7) under visible-light irradiation. It is found that the composites exhibit much higher photocatalytic efficiency than bare $BiFeO_3$. Meanwhile, the intrinsical visible-light-driven photocatalytic activity of Ag_3PO_4/$BiFeO_3$ composites was further confirmed by the degradation of phenol. In addition, the photo-Fenton-like catalysis property of the composite was also evaluated. The photocurrent analysis indicates that the combination of $BiFeO_3$ with Ag_3PO_4 leads to the inhibition of recombination of photoinduced electrons and holes. The obvious enhancement in the photocatalytic activity of the composite is mainly ascribed to the efficient photogenerated charge separation and interfacial charge migration caused by the formation of Ag_3PO_4/$BiFeO_3$ p-n heterojunctions.

Keywords: $BiFeO_3$, Ag_3PO_4, Heterojunction, Photocatalysis,

PACS: 81.05.Hd82.65.+r82.50.–m

Background

Recently, the semiconductor photocatalysis has received considerable attention as a promising technology for energy conversion and pollution treatment [1–3]. As we know, the widely investigated photocatalyst TiO_2 is merely active under ultraviolet (UV) light irradiation which only constitutes about 5% of solar light and thus greatly limits its photocatalytic applications under sunlight. Consequently, it is necessary to develop the visible-light-driven photocatalysts [4–8].

Bismuth- or ferrum-based semiconductor oxides generally possess a moderate bandgap energy (~ 2.0 eV) and are regarded as an important class of visible-light-responsive photocatalysts [9–19]. Among them, $BiFeO_3$ with a perovskite-type structure is found to exhibit interesting photocatalytic performance for the dye degradation and water splitting under visible-light irradiation [20–25]. However, its photocatalytic activity is not impressive due to the high recombination rate of photogenerated electrons (e^-) and holes (h^+). Fortunately, it is demonstrated that coupling of $BiFeO_3$ with a narrow-bandgap semiconductor of matched band edge potentials to form a heterojunction is one of the most promising strategies to promote the separation of photogenerated charges, thus leading to improved photocatalytic activity of $BiFeO_3$ [26–31]. For example, Chaiwichian et al. reported that $BiFeO_3$-Bi_2WO_6 nanocomposites exhibited enhanced activity in dye degradation [29]. Wang et al. observed that AgCl/Ag/$BiFeO_3$ showed much higher visible-light photocatalytic activity than bare $BiFeO_3$ [30]. Fan and co-workers found that the combination of g-C_3N_4 with $BiFeO_3$ can obviously improve the catalytic activity compared with pure $BiFeO_3$ [31].

* Correspondence: hyang@lut.cn
[1]State Key Laboratory of Advanced Processing and Recycling of Non-ferrous Metals, Lanzhou University of Technology, Lanzhou 730050, China
Full list of author information is available at the end of the article

Silver orthophosphate (Ag_3PO_4), as an excellent visible-light-driven photocatalyst, has attracted considerable attention in the photocatalytic field [32–37]. It has been shown that Ag_3PO_4 can achieve extremely high quantum yield (~ 90%) for oxygen generation from water splitting [32, 33]. Furthermore, it possesses superior photooxidation capability for organic pollution degradation due to its highly positive valence band position [34]. In most cases, owing to its appropriate energy band position and narrow bandgap, Ag_3PO_4 is widely employed as the cocatalyst to combine with other photocatalysts to form composites, leading to an obvious improvement of photocatalytic behavior, such as Ag_3PO_4/Bi_2WO_6, Ag_3PO_4/$BiPO_4$, Ag_3PO_4/$Bi_2O_2CO_3$, Ag_3PO_4/g-C_3N_4, Ag_3PO_4/$BiVO_4$, $Bi_4Ti_3O_{12}$/Ag_3PO_4, Ag_3PO_4/$ZnFe_2O_4$, Ag_3PO_4/WO_3, Ag_3PO_4/ZnO, and Bi_2MoO_6/Ag_3PO_4 [38–47]. It is reported that $BiFeO_3$ is an n-type semiconductor and Ag_3PO_4 is known as a p-type semiconductor [43, 48]. The construction of Ag_3PO_4/$BiFeO_3$ p-n heterojunction composites may be a feasible method to obtain efficient photocatalyst. However, to the best of our knowledge, little work has been devoted to the investigation of photocatalytic performance of Ag_3PO_4/$BiFeO_3$ composites.

In this work, Ag_3PO_4/$BiFeO_3$ p-n heterojunction composites were facilely prepared via the precipitation of Ag_3PO_4 microparticles on the $BiFeO_3$ microcuboids. Acid orange 7 (AO7) and phenol were selected as the model pollutant to evaluate the photocatalytic activity of the composites under visible-light irradiation. Moreover, the photo-Fenton-like catalysis activity of the composite was also investigated. The underlying mechanism of the composites for the degradation of organic pollutants was discussed.

Methods

Preparation of Ag_3PO_4/$BiFeO_3$ Composites

$BiFeO_3$ microcuboids were synthesized via a hydrothermal route. 0.005 mol of $Bi(NO_3)_3$•$5H_2O$ and 0.005 mol of $Fe(NO_3)_3$•$9H_2O$ were dissolved in 20 mL of dilute nitric acid solution (5 mL HNO_3 + 15 mL deionized water). Sixty milliliters of KOH solution with concentration of 4.5 mol/L was added to the above solution drop by drop under magnetic stirring. After 8 min of ultrasonic treatment and another 30 min of vigorous magnetic stirring, the mixture solution was sealed in a Teflon-lined stainless steel autoclave of 100 mL capacity and submitted to hydrothermal reaction at 200 °C for 6 h. After the autoclave was cooled naturally to room temperature, the precipitate was collected by centrifugation, washed with deionized water (two times) and absolute ethanol (three times), and then dried at 80 °C for 12 h to obtain final $BiFeO_3$ product. Ag_3PO_4 microparticles were prepared by a precipitation method. Three millimoles of $AgNO_3$ was dissolved into 30 mL deionized water, and 1 mmol Na_3PO_4·$12H_2O$ was added into 30 mL deionized water with the aid of magnetic stirring. After the solution was homogeneous, the latter solution was added dropwise into the former under vigorous magnetic stirring for 7 h. During the reaction, the color of the solution changed into yellow. Finally, the mixture was centrifuged to collect the precipitate. The obtained precipitate was washed several times with deionized water and then dried in a vacuum oven at 60 °C for 8 h.

Ag_3PO_4/$BiFeO_3$ composites were synthesized as follows: 0.1 g of $BiFeO_3$ microcuboids were dispersed in 30 mL deionized water and then ultrasonicated for 2 h. After that, a certain amount of $AgNO_3$ was dissolved into the above suspension. To this mixture was added drop by drop a certain concentration of Na_3PO_4 solution (30 mL) under vigorous magnetic stirring for 7 h. The as-obtained composites were separated by centrifugation, washed repeatedly with deionized water, and dried in a vacuum oven at 60 °C for 8 h. To investigate the effect of Ag_3PO_4 content on the photocatalytic property of obtained composites, a series of sample was fabricated with different Ag_3PO_4 mass ratios of 5%, 10%, 20%, and 40% and the corresponding samples were termed as 5wt%Ag_3PO_4/$BiFeO_3$, 10wt%Ag_3PO_4/$BiFeO_3$, 20wt%Ag_3PO_4/$BiFeO_3$, and 40wt%Ag_3PO_4/$BiFeO_3$, respectively. For comparison, the composite termed as 20wt%Ag_3PO_4/$BiFeO_3$-M was also prepared by direct mechanical mixing of $BiFeO_3$ microcuboids and Ag_3PO_4 microparticles, where Ag_3PO_4 occupies a mass fraction of 20% in the composite.

Photoelectrochemical Measurements

The photocurrent test was carried out on the electrochemical workstation (CST 350) with a three-electrode cell as described in the literature [49]. In this three-electrode system, a platinum foil and a standard calomel electrode were used as the counter electrode and reference electrode, respectively. The working electrode was fabricated as follows: 15 mg photocatalysts, 0.75 mg carbon black, and 0.75 mg polyvinylidene fluoride (PVDF) were added into 1-methyl-2-pyrrolidione (NMP) to produce slurry, which was then uniformly coated on a 1.0 × 1.0 cm^2 fluoride-doped tin oxide glass electrode. After that, the electrode was dried at 60 °C for 5 h. A 300-W Xe lamp with a 420-nm cut-off filter was employed as the visible light source. The photoelectrochemical measurement was performed in the 0.1-M Na_2SO_4 electrolyte solution, and its pH value was measured to be ~ 5.3.The photocurrent-time (I-t) curves were measured at a fixed bias potential of 0.2 V. The electrochemical impedance spectroscopy

(EIS) test was performed by using the sinusoidal voltage pulse with amplitude of 5 mV and in the frequency range from 10^{-2} to 10^{5} Hz.

Photocatalytic Activity Test

The photocatalytic activity of samples was evaluated toward the degradation of AO7 and phenol under visible-light irradiation. Typically, the initial AO7 or phenol concentration was 5 mg/L with a catalyst loading of 0.5 g/L. The pH values of AO7 and phenol solution were measured to be ~ 6.8 and ~ 6.2, respectively. Prior to illumination, the mixture was stirred in the dark for 0.5 h to achieve the adsorption-desorption equilibrium of organic molecule on the surface of catalysts. This reaction solution was then exposed to a 300-W xenon lamp with a 420-nm cut-off filter, and the corresponding light intensity was measured to be ~ 50 mW cm^{-2}. During the photocatalytic experiment, a small amount of reaction solution was collected at the given time intervals and then centrifuged to separate catalysts. The concentration of AO7 or phenol was determined by detecting the absorbance of the supernatant at a given wavelength ($\lambda_{AO7} = 484$ nm and $\lambda_{phenol} = 270$ nm) using a UV-visible spectrophotometer. To evaluate the photocatalytic reusability of the photocatalysts, the recycling experiment for the degradation of AO7 was performed. After the first photocatalytic test was completed, the photocatalysts were collected by centrifugation, washed with distilled water, and dried. The collected photocatalysts were added into the fresh dye solution for the next cycle of the photocatalytic experiment. To investigate the photo-Fenton-like catalysis ability of the photocatalysts, H_2O_2 (5 mmol/L) was added into the reaction solution. The photo-Fenton-like experiment procedure was similar to the above photocatalytic process.

Characterization

The phase purity of the samples was investigated by X-ray diffractometer (XRD, Bruker D8 Advanced) using Cu Kα radiation. The morphology of the samples was observed by a field-emission scanning electron microscope (SEM, JEOL JSM-6701F) and field-emission transmission electron microscope (TEM, JEOL JEM-2010). The composition of the samples was measured by energy dispersive X-ray spectroscopy. The chemical state of the element was tested using X-ray photoelectron spectroscopy (XPS, PHI-5702), where the binding energy scale of the XPS data was calibrated against the adventitious C 1s peak at the binding energy of 284.8 eV. The ultraviolet-visible (UV-vis) diffuse reflectance spectra of the products were obtained using a UV-vis spectrophotometer (PERSEE TU-1901) with $BaSO_4$ as a reference. The PL spectra of the samples were recorded on a fluorescence spectrophotometer (SHIMADZU RF-6000) with the excitation wavelength of ~ 350 nm.

Results and Discussion

XRD Analysis

Figure 1 presents the XRD patterns of $BiFeO_3$, Ag_3PO_4, and $Ag_3PO_4/BiFeO_3$ composites with different Ag_3PO_4 contents. For bare $BiFeO_3$ sample, all the diffraction peaks match well with the rhombohedral structure of $BiFeO_3$ (PDF card no. 74-2016), and for bare Ag_3PO_4

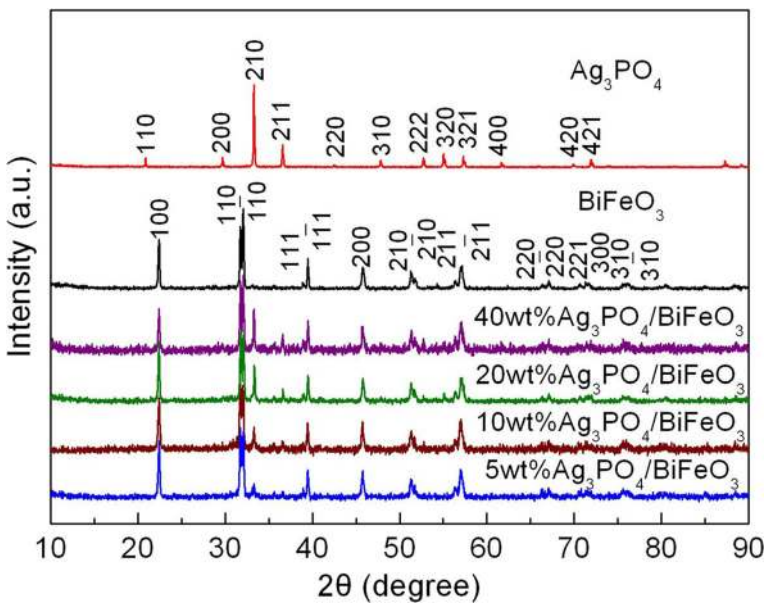

Fig. 1 XRD patterns of $BiFeO_3$, Ag_3PO_4, and $Ag_3PO_4/BiFeO_3$ composites

sample, the diffraction peaks can be perfectly indexed to cubic Ag_3PO_4 phase (PDF card no. 06-0505); this indicates that high-purity $BiFeO_3$ and Ag_3PO_4 have been successfully prepared. In the case of the composites, the XRD patterns can be assigned to the characteristic diffraction peaks of $BiFeO_3$ and Ag_3PO_4, and no diffraction peaks of impurity appear in the patterns. Moreover, it is seen that by increasing the content of Ag_3PO_4, the intensity of the characteristic peaks of Ag_3PO_4 increases gradually. The results suggest that the composites consist of rhombohedral $BiFeO_3$ and cubic Ag_3PO_4, and no other phase is generated during the preparation of the composites.

Morphology Observation

The morphology of the samples was observed by SEM and TEM. Figure 2a, b shows the SEM image and TEM image of bare $BiFeO_3$, revealing that the prepared $BiFeO_3$ particles exhibit cuboid-like shape with 200–500 nm in size and have a smooth surface. The inset of Fig. 2a displays the length-to-width ratio distribution of $BiFeO_3$ particles, which reveals that the length-to-width ratio

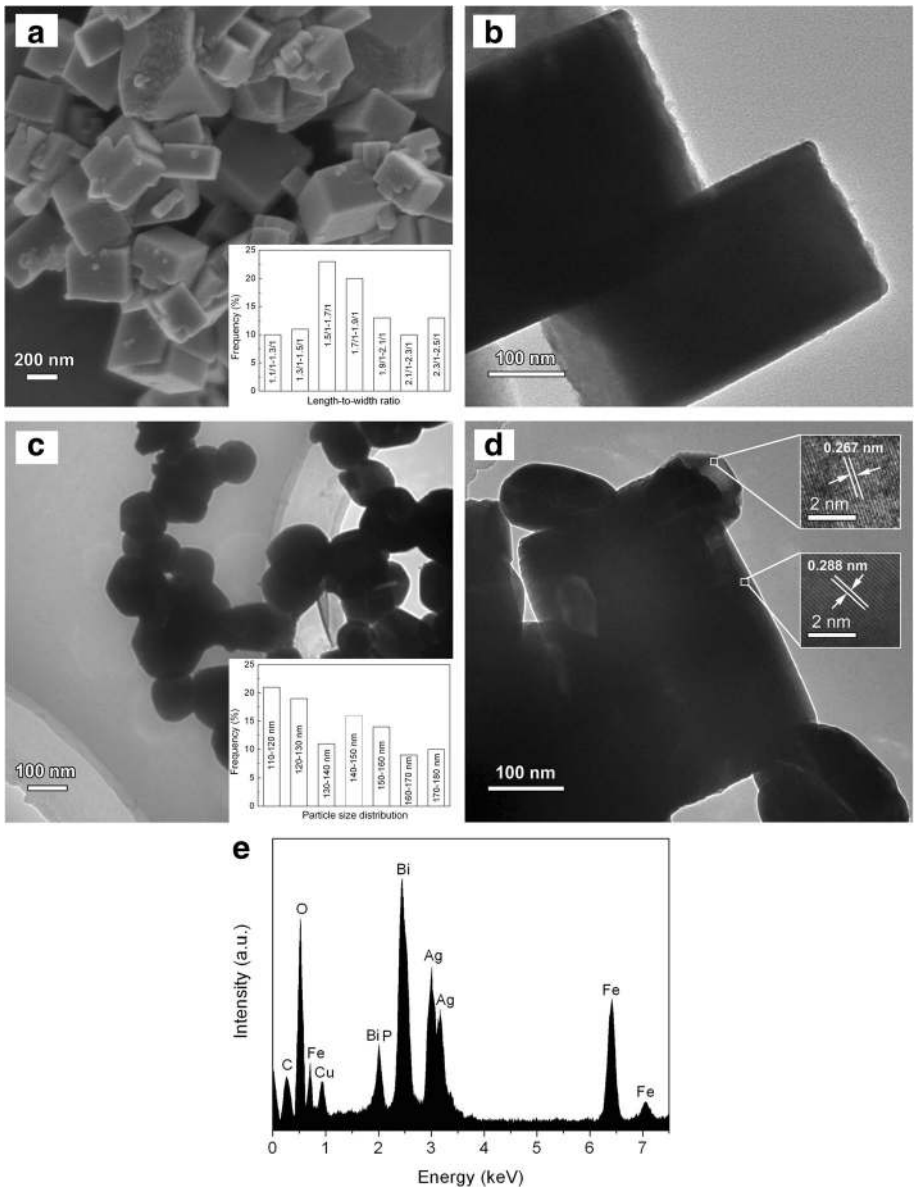

Fig. 2 **a** SEM (the inset is the length-to-width ratio distribution of $BiFeO_3$ microcuboids) and **b** TEM image of $BiFeO_3$ microcuboids. TEM image of **c** Ag_3PO_4 microparticles (the inset is the size distribution of Ag_3PO_4 microparticles) and **d** 20wt%Ag_3PO_4/$BiFeO_3$ sample; inset shows its HRTEM image. **e** EDX spectrum of 20wt%Ag_3PO_4/$BiFeO_3$ sample

ranges from 1.1/1 to 2.5/1. As can be seen from the TEM image in Fig. 2c, bare Ag_3PO_4 consists of irregular sphere-like particles. The size distribution of Ag_3PO_4 particles is shown in the inset of Fig. 2c, indicating a wide distribution of particle size ranging from 110 to 180 nm. From the TEM image of the 20wt%Ag_3PO_4/$BiFeO_3$ composite (Fig. 2d), one can see that the irregular microspheres are attached to the cuboid-shaped particle. The high-resolution TEM (HRTEM) images obtained from the different particles indicate two distinct sets of lattice fringes (insets in Fig. 2d). The interplanar spacing of ~ 0.288 nm matches the $BiFeO_3$ (110) planes, whereas the interplanar distance of ~ 0.267 nm corresponds to the Ag_3PO_4 (210) planes. In addition, the EDX analysis suggests that the composite includes all the elements of Ag_3PO_4 and $BiFeO_3$ phases (Fig. 2e). The observed C and Cu signals in the EDX spectrum of Fig. 2e could arise from the microgrid used for supporting the sample [50]. These results reveal that Ag_3PO_4 particles are decorated on the surface of $BiFeO_3$ microcuboids, resulting in the formation of Ag_3PO_4/$BiFeO_3$ p-n heterostructures.

XPS Analysis

The XPS analysis was performed to reveal the chemical states of $BiFeO_3$ and 20wt%Ag_3PO_4/$BiFeO_3$, as shown in Fig. 3. Figure 3a shows the high-resolution XPS spectrum of Ag 3d in the composite. The two obvious peaks at

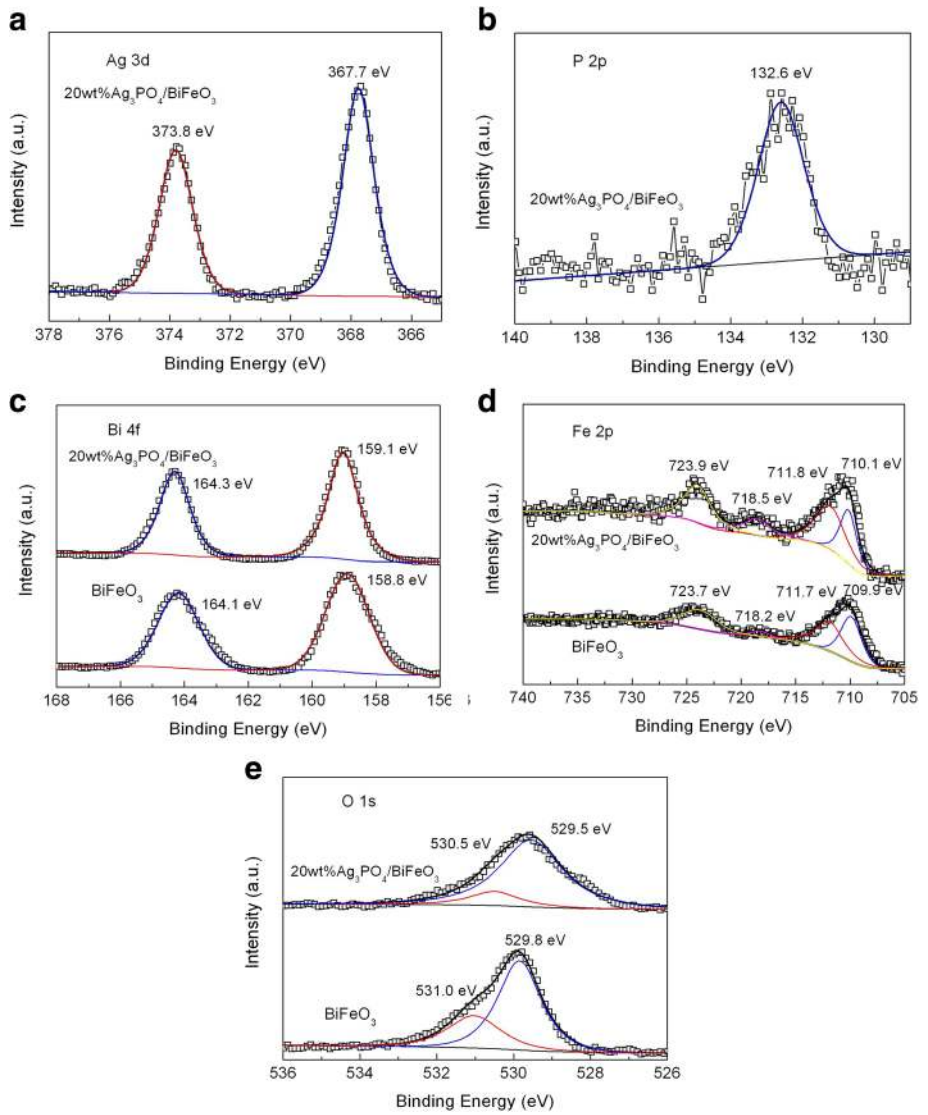

Fig. 3 High-resolution XPS spectra of $BiFeO_3$ and 20wt%Ag_3PO_4/$BiFeO_3$ sample. **a** Ag 3d and **b** P 2p of 20wt%Ag_3PO_4/$BiFeO_3$ sample. **c** Bi 4f, **d** Fe 2p, and **e** O1s of $BiFeO_3$ and 20wt%Ag_3PO_4/$BiFeO_3$ sample

373.8 and 367.7 eV are attributed to the Ag $3d_{3/2}$ and Ag $3d_{5/2}$ binding energies of Ag^+. Figure 3b presents the P 2p high-resolution XPS spectrum of the composite. The peak at around 133.2 eV corresponds to the characteristic binding energy of P^{5+} oxidation state in Ag_3PO_4 [51]. Figure 3c, d, shows the Bi 4f and Fe 2p high-resolution XPS spectra, respectively. For bare $BiFeO_3$, the Bi 4f spectrum shows two strong peaks at binding energies of 164.1 eV and 158.8 eV, belonging to the Bi $4f_{5/2}$ and Bi $4f_{7/2}$, respectively, which indicates that Bi ion possesses the oxidation state of + 3. For Fe 2p spectrum, the peak located at 723.7 eV is assigned to the Fe $2p_{1/2}$ of Fe^{3+}. Another strong XPS signal at ~ 711.6 eV can be fitted into two peaks at 711.7 and 709.9 eV. The peak at 709.9 eV corresponds to the binding energy of Fe $2p_{3/2}$ of Fe^{2+}. The binding energy at 711.7 eV belongs to the Fe $2p_{3/2}$ of Fe^{3+}. In addition, a satellite peak is found at around 718.2 eV, which is attributed to the mixed oxidation states of Fe. From the XPS analysis of the Fe element, it can be seen that Fe exists in the form of Fe^{3+} and Fe^{2+} in bare $BiFeO_3$. It is worth noting that the Bi 4f and Fe 2p binding energies in 20wt%Ag_3PO_4/$BiFeO_3$ exhibit a slight shift in comparison to bare $BiFeO_3$, which is mainly attributed to the interaction between $BiFeO_3$ and Ag_3PO_4. Figure 3e displays the O 1s high-resolution XPS spectra of $BiFeO_3$ and 20wt%Ag_3PO_4/$BiFeO_3$. For bare $BiFeO_3$, the O 1s signal can be divided into two peaks at 529.8 and 531.0 eV. The binding energy of 529.8 eV corresponds to the lattice oxygen while the small peak at higher binding energy of 531.0 eV is caused by surface defects and chemisorbed oxygen species. Compared with bare $BiFeO_3$, the O 1s peak in the composite experiences a shift, which is also due to the interaction between Ag_3PO_4 and $BiFeO_3$.

Optical Absorption Property

The optical absorption behavior of the samples was investigated by measuring their UV-vis diffuse reflectance spectra, as presented in Fig. 4a. The corresponding absorption spectra transformed from the diffuse reflectance spectra according to the Kubelka-Munk (K-M) theory is shown in Fig. 4b [52]. It is seen that all the samples exhibit an important light absorption at $\lambda <$ 600 nm. In order to obtain the absorption edge of the samples, the first derivative of the reflectance (R) with respect to wavelength λ (i.e., $dR/d\lambda$) was carried out, as shown in Fig. 4c. The absorption edge can be determined from the peak wavelength in the derivative spectra [53]. It can be seen that the light absorption edge of bare Ag_3PO_4 is located at ~ 527 nm, corresponding to the bandgap energy (E_g) of ~ 2.35 eV. Bare $BiFeO_3$ exhibits an absorption edge at around 567 nm, corresponding to the E_g of ~ 2.18 eV. In addition to the absorption edge, a weak peak at ~ 700 nm is observed, which is probably attributed to the existence of surface states in the middle of the bandgap of $BiFeO_3$. When coupled with Ag_3PO_4, the absorption edge of $BiFeO_3$ does not undergo obvious change, which indicates that the introduction of Ag_3PO_4 has no apparent effect on the bandgap structure of $BiFeO_3$.

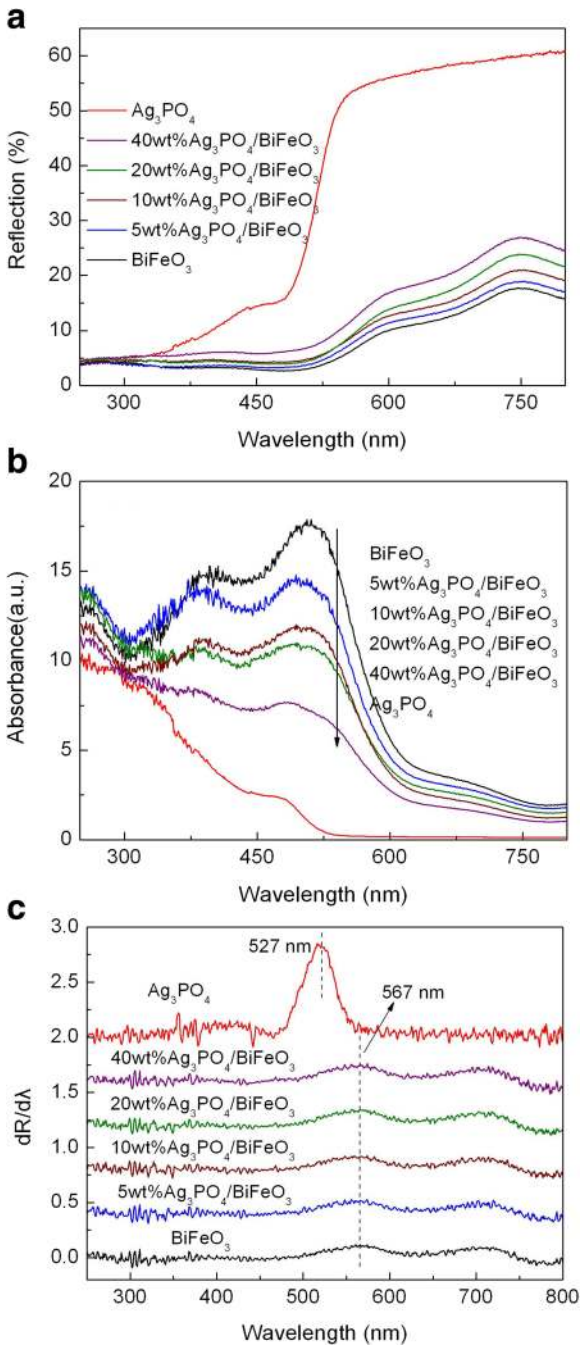

Fig. 4 **a** UV-visible diffuse reflectance spectra of $BiFeO_3$, Ag_3PO_4, and Ag_3PO_4/$BiFeO_3$ composites. **b** The corresponding absorption spectra and **c** the corresponding first derivative of the diffuse reflectance spectra

Photocatalytic Activity Measurement

AO7 was selected as a target pollutant for evaluating the photocatalytic performance of the samples. The photocatalytic degradation of AO7 was investigated under visible-light irradiation, and the result is shown in Fig. 5. Prior to photocatalytic reaction, blank and absorption experiments were performed. It is seen that no obvious degradation of dye is detected under irradiation without the catalysts or in the presence of catalysts without irradiation, suggesting that self-degradation and absorption of AO7 during the photocatalytic process are negligible. Bare $BiFeO_3$ has weak photocatalytic activity, and only ~ 27% of AO7 is degraded with 120 min of irradiation. When $BiFeO_3$ microcuboids are combined with Ag_3PO_4 microparticles, the formed $Ag_3PO_4/BiFeO_3$ composites exhibit superior photocatalytic activity to bare $BiFeO_3$. After 120 min of exposure, the degradation percentage of AO7 over the samples is in the order 40wt%$Ag_3PO_4/BiFeO_3$ (~ 91%) > 20wt%$Ag_3PO_4/BiFeO_3$ (~ 87%) > 10wt%$Ag_3PO_4/BiFeO_3$ (~ 69%) > 5wt%$Ag_3PO_4/BiFeO_3$ (~ 46%) > $BiFeO_3$ (~ 27%). It is found that the photocatalytic performance of the composites exhibit an increasing trend with the increase of Ag_3PO_4 content. Among these composites, the photocatalytic efficiency of 40wt%$Ag_3PO_4/BiFeO_3$ is very close to that of 20wt%$Ag_3PO_4/BiFeO_3$. Thus, in the present study, the most appropriate mass ratio of Ag_3PO_4 can be considered as 20% in the composites. Moreover, it is worth noting that the mechanical mixture sample 20wt%$Ag_3PO_4/BiFeO_3$-M exhibits much lower photocatalytic activity than 20wt%$Ag_3PO_4/BiFeO_3$. This reveals that the construction of heterojunction between $BiFeO_3$ and Ag_3PO_4 is necessary for the enhancement of photocatalytic activity. Moreover, compared with $BiFeO_3$/a-Fe_2O_3 and $BiFeO_3$-Bi_2WO_6 composites [26, 29], the $Ag_3PO_4/BiFeO_3$ heterojunction composites prepared in the present study manifest a higher photocatalytic activity toward the dye degradation.

To further confirm the photocatalytic property of the composites, the photocatalytic degradation of colorless phenol over 20wt%$Ag_3PO_4/BiFeO_3$ and $BiFeO_3$ under visible-light irradiation was also investigated. As shown in Fig. 6, the self-degradation and absorption of phenol can be neglected based on the results of blank and absorption experiments. It can be seen that just ~ 9% of phenol is degraded catalyzed by $BiFeO_3$ after 120 min of exposure. Whereas, when 20wt%$Ag_3PO_4/BiFeO_3$ is used as the photocatalyst, the degradation percentage of phenol can be obviously enhanced under the same conditions. The result suggests that the degradation of the dye on the visible-light-irradiated $Ag_3PO_4/BiFeO_3$ composites is attributed to their intrinsical photocatalytic activity instead of dye sensitization.

To evaluate the reusability of the photocatalysts, the recycling photocatalytic degradation experiments of AO7 over 20wt%$Ag_3PO_4/BiFeO_3$ and Ag_3PO_4 were carried out under the same photocatalytic conditions. As shown in Fig. 7, after three successive recycling runs, the composite still exhibits relatively high photocatalytic activity, while the degradation

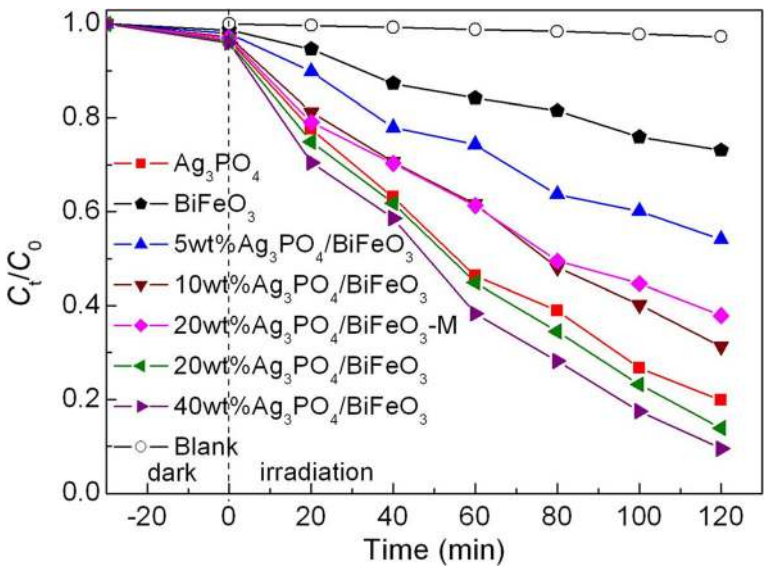

Fig. 5 Photocatalytic activities of $BiFeO_3$ and $Ag_3PO_4/BiFeO_3$ composites toward the degradation of AO7 under visible-light irradiation, along with the blank and absorption experiment results

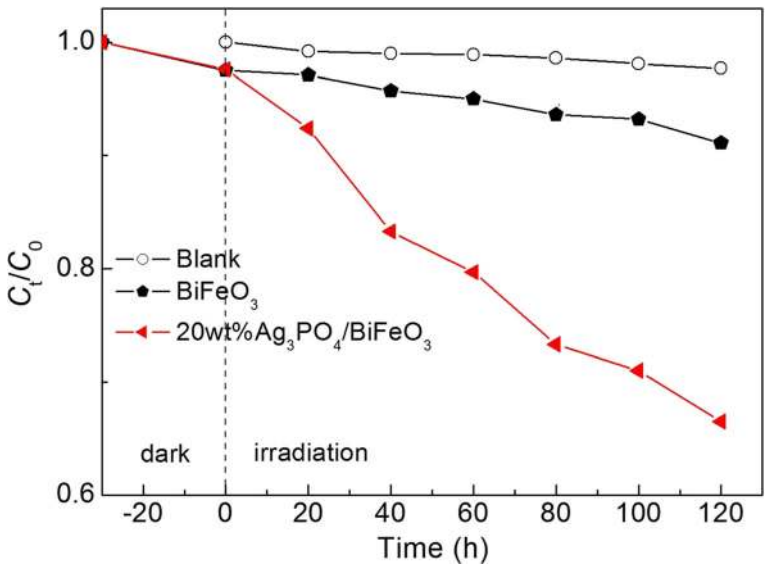

Fig. 6 Photocatalytic degradation of phenol over $BiFeO_3$ and 20wt%Ag_3PO_4/$BiFeO_3$ sample under visible-light irradiation, along with the blank and absorption experiment result

efficiency over Ag_3PO_4 undergoes an obvious decrease. Figure 8a, b shows the TEM image and XRD pattern of the composite after cycling experiment, respectively. It is clear that Ag_3PO_4 microparticles are still assembled on the surface of $BiFeO_3$ microcuboids without destruction of the heterostructures, and no obvious crystal structure change is observed. This suggests that Ag_3PO_4/$BiFeO_3$ p-n heterojunction composites possess good photocatalytic reusability.

Photo-Fenton-like Catalytic Activity

Apart from its photocatalytic property, $BiFeO_3$ also exhibits prominent photo-Fenton-like catalysis ability [54–56]. Figure 9 shows the photo-Fenton-like degradation of AO7 over 20wt%Ag_3PO_4/$BiFeO_3$ and $BiFeO_3$ in the presence of H_2O_2. Compared with the reaction systems without H_2O_2, the introduction of H_2O_2 remarkably enhances the degradation percentage of the dye. This result is mainly due to the

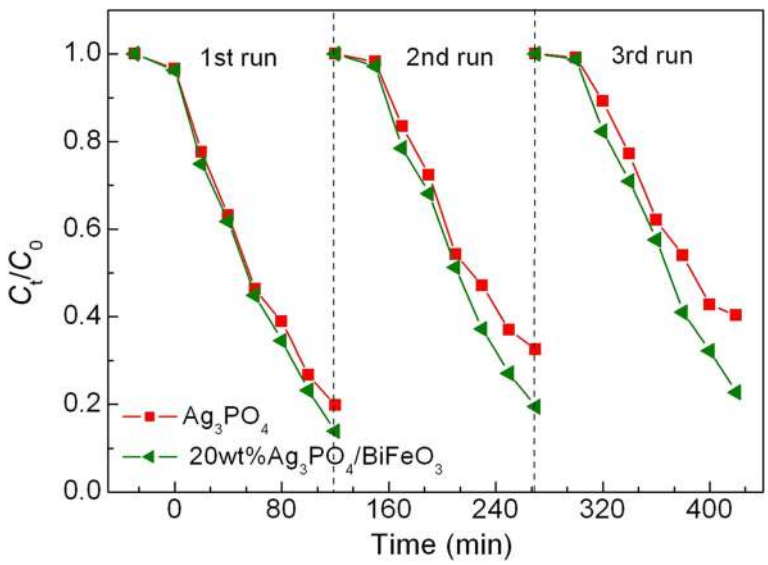

Fig. 7 Photocatalytic degradation of AO7 over Ag_3PO_4 and 20wt%Ag_3PO_4/$BiFeO_3$ sample during three cycles

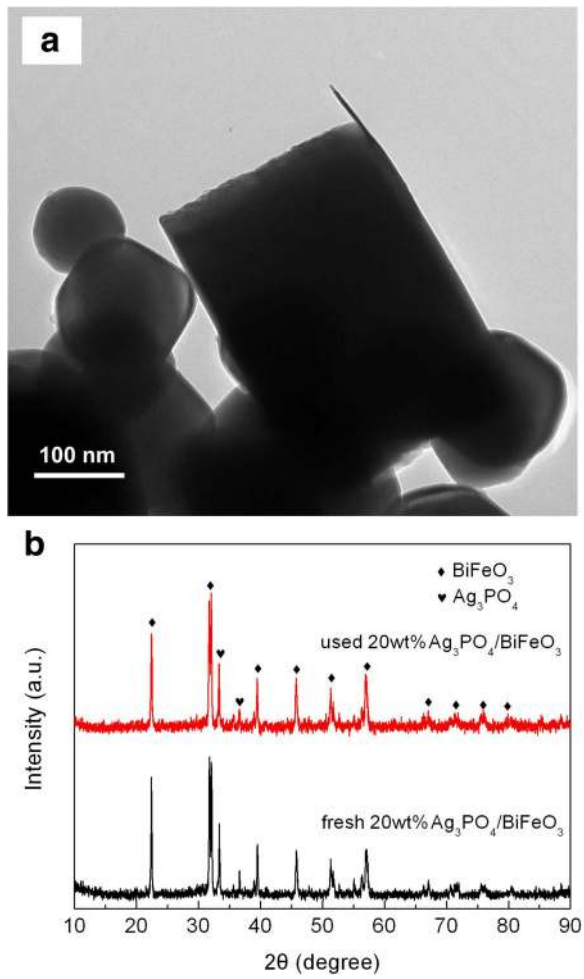

Fig. 8 **a** TEM image and **b** XRD pattern of 20wt%Ag_3PO_4/$BiFeO_3$ sample after cycling photocatalytic experiments

photo-Fenton-like reaction mechanism. In the presence of visible-light irradiation and H_2O_2, Fe^{3+} on the surface of $BiFeO_3$ can be converted to Fe^{2+} with the generation of hydroxyl (•OH) radicals (Eq. 1). Consequently, Fe^{2+} can react with H_2O_2 to produce Fe^{3+} and •OH (Eq. 2). During the above cycle reaction, more •OH is produced, which is generally considered to be a primary active species for the dye degradation (as evidenced by active species trapping experiment given in Fig. 11). In the case of bare $BiFeO_3$, the high recombination rate of the photogenerated charges limits the yield of photogenerated electrons, which tends to suppress the reduction of Fe^{3+} into Fe^{2+}(Eq. 3). This leads to the limited enhancement of degradation percentage. For Ag_3PO_4/$BiFeO_3$ composites, photogenerated electrons and holes can be efficiently separated, and thus, more photogenerated electrons are available for promoting the quick conversion from Fe^{3+} into Fe^{2+} (Eq. 3) [57]. Benefitting from this electron reduction, the photo-Fenton process for the composites is more efficient than that for bare $BiFeO_3$. As a result, Ag_3PO_4/$BiFeO_3$ p-n heterojunction composites manifest much enhanced photo-Fenton performance.

$$Fe^{3+} + H_2O + h\nu \rightarrow Fe^{2+} + \bullet OH + H^+ \quad (1)$$

$$Fe^{2+} + H_2O_2 \rightarrow Fe^{3+} + \bullet OH + OH^- \quad (2)$$

$$Fe^{3+} + e^- \rightarrow Fe^{2+} \quad (3)$$

Photogenerated Charge Performance

To evaluate the separation behavior of photogenerated charges of the samples, transient photocurrent responses, ESI spectra, and PL spectra of $BiFeO_3$ and 20wt%Ag_3PO_4/$BiFeO_3$ were measured. Figure 10a shows the photocurrent-time (I-t) curves of the photocatalysts under intermittent visible-light irradiation with several on-off cycles. It can be seen that the photocurrent value of the composite is much higher than that of bare $BiFeO_3$, indicating that the construction of Ag_3PO_4/$BiFeO_3$ p-n heterojunctions is beneficial to inhibit the recombination of photogenerated electrons and holes. Figure 10b presents the ESI spectra of the samples. One can see that the composite exhibits smaller impedance arc radii compared with $BiFeO_3$, which suggests the lower charge transfer resistance of the composite. These results reveal that the separation and migration of the photogenerated charges can be improved in the composite, thus providing more photoinduced holes and electrons for the photocatalysis. Figure 10c shows the Mott-Schottky plot at frequency of 3000 Hz for Ag_3PO_4. The negative slope of the plot indicates that Ag_3PO_4 is a p-type semiconductor, which is consistent with the report [43]. The PL spectra of $BiFeO_3$ and 20wt%Ag_3PO_4/$BiFeO_3$ are shown in Fig. 10d. The two samples exhibit obvious emission peaks at ~ 522 nm, which are mainly attributed to the recombination of the photogenerated electron/hole pairs. It is worth noting that the PL intensity of the composite is much smaller than that of bare $BiFeO_3$. This further confirms that the construction of Ag_3PO_4/$BiFeO_3$ heterojunction promotes the separation of photoinduced charges.

Active Species Trapping

It is well known that photogenerated hole (h^+), hydroxyl (•OH), and superoxide ($\bullet O^{2-}$) are considered to the main active species responsible for the photocatalytic degradation of dye. In order to clarify the role of the active species in the present photocatalytic system, the active species trapping experiments were carried out, as shown in Fig. 11.

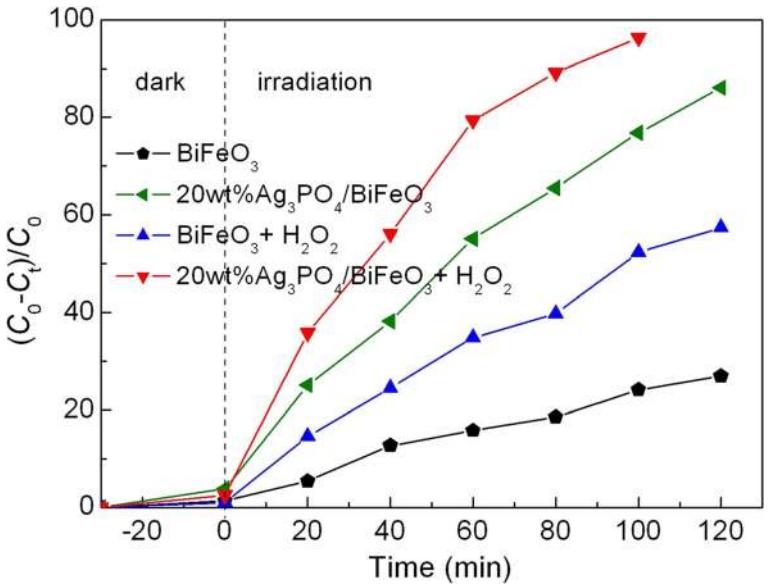

Fig. 9 Photocatalytic activities of $BiFeO_3$ and 20wt%Ag_3PO_4/$BiFeO_3$ sample toward the degradation of AO7 under visible-light irradiation in the presence of H_2O_2

It can be seen that the degradation percentage of AO7 undergoes an obvious decrease after the introduction of ethanol (scavenger of •OH, 10% by volume) or ethylene diamine tetraacetic acid (EDTA, scavenger of h^+, 2 mM). This indicates that •OH and h^+ are the major active species involved in the photocatalytic reaction. After the addition of benzoquinone (BQ, scavenger of $•O^{2-}$, 1 mM), a slight decrease of degradation percentage is detected, suggesting that $•O^{2-}$ plays a relatively minor role in the dye degradation.

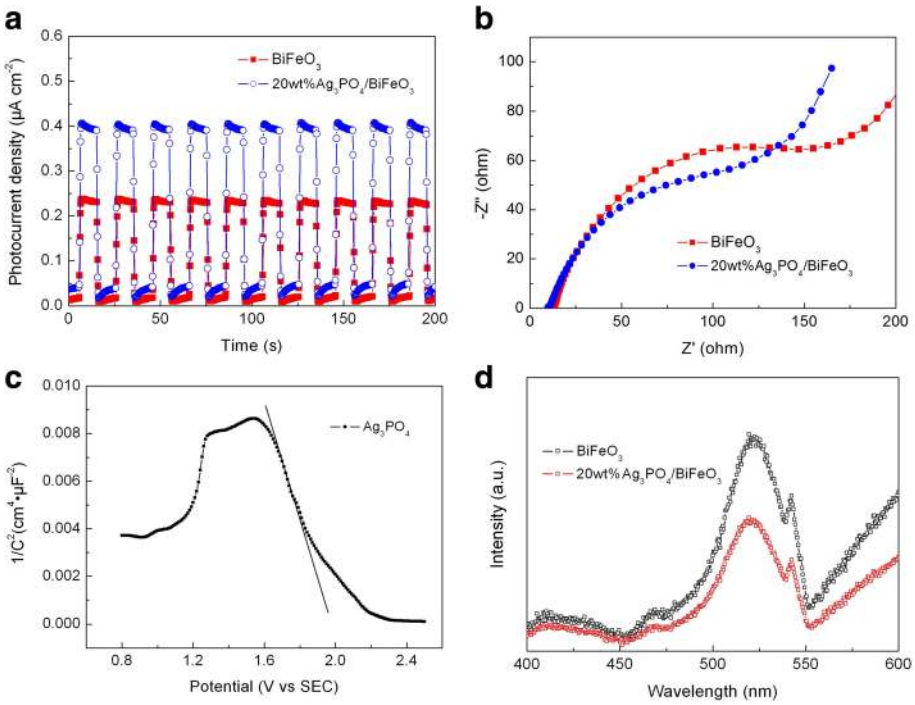

Fig. 10 **a** Transient photocurrent response and **b** EIS spectra of $BiFeO_3$ and 20wt%Ag_3PO_4/$BiFeO_3$ sample. **c** Mott-Schottky plot of Ag_3PO_4. **d** PL spectra of $BiFeO_3$ and 20wt%Ag_3PO_4/$BiFeO_3$ samples

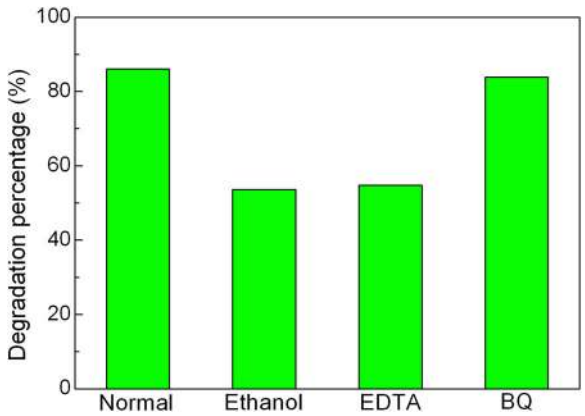

Fig. 11 Effects of ethanol, EDTA, and BQ on the degradation percentage of AO7 over 20wt%Ag_3PO_4/$BiFeO_3$ composite

Proposed Photocatalytic Mechanism

It is well known that the redox ability and migration of photogenerated charges are highly related to the energy-band potentials of photocatalysts. The valence band (VB) and conduction band (CB) of $BiFeO_3$ and Ag_3PO_4 can be obtained using the following equation [58, 59]:

$$E_{VB} = X - E^e + 0.5E_g \quad (4)$$

$$E_{CB} = X - E^e - 0.5E_g \quad (5)$$

X is the absolute electronegativity of semiconductor (calculated as the arithmetic mean of the electron affinity and the first ionization of the constituent atoms). E^e is the energy of free electrons on the hydrogen scale (~ 4.5 eV). The X values of $BiFeO_3$ and Ag_3PO_4 are estimated to be 5.93 and 5.98 eV, respectively [43, 60]. Based on Eqs. (4) and (5), the CB/VB potentials of $BiFeO_3$ and Ag_3PO_4 are calculated to be 0.34/2.52 V and 0.31/2.66 V vs. NHE, respectively. The energy-band potential diagram of the two photocatalysts is shown in Fig. 12a. It is reported that $BiFeO_3$ is an n-type semiconductor and its Fermi level lies close to the CB [48]. Ag_3PO_4 is demonstrated to be a p-type semiconductor (see Fig. 10c), whose Fermi energy level is close to the VB [43].When $BiFeO_3$ is combined with Ag_3PO_4 to form p-n heterojunction (see Fig. 12b), the diffusion of electrons and holes between the two photocatalysts will build an internal electric field at the interface region of the p-n heterojunction with direction from $BiFeO_3$ to Ag_3PO_4. Simultaneously, the energy-band potential of $BiFeO_3$ tends to move down along with its Fermi level whereas that of Ag_3PO_4 tends to raise up accompanied by its Fermi level until an equilibrium state of Fermi level of the two photocatalysts is achieved. Upon visible-light irradiation, both $BiFeO_3$ and Ag_3PO_4 can be excited to generate photoinduced electron and hole pairs. Under the promotion of the internal electric field, the photogenerated electrons in the CB of Ag_3PO_4 will migrate to the CB of $BiFeO_3$, while the photogenerated holes will transfer from the VB of $BiFeO_3$ to that of Ag_3PO_4. As a result, the recombination of photogenerated charges can be effectively inhibited, as evidenced by the photocurrent and PL analysis (see Fig. 10a, d). Thus, more photogenerated electrons and holes can participate in the photocatalytic redox reaction, leading to the enhancement of the photocatalytic activity for the Ag_3PO_4/$BiFeO_3$ p-n heterojunction composites.

Conclusions

Ag_3PO_4/$BiFeO_3$ p-n heterojunction composites were synthesized through the decoration of Ag_3PO_4 spherical-like microparticles on the surface of $BiFeO_3$ microcuboids. Compared with bare $BiFeO_3$, the as-obtained composites exhibit enhanced

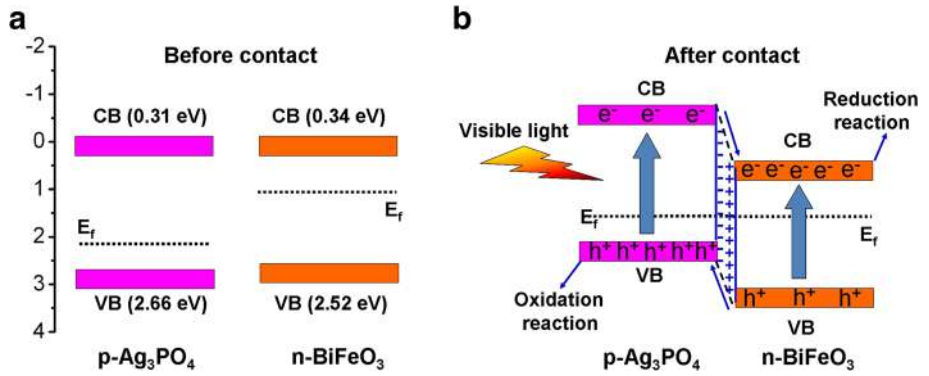

Fig. 12 Schematic illustration of proposed photocatalytic mechanism for Ag_3PO_4/$BiFeO_3$ composite. **a** Before contact. **b** After contact

visible-light photocatalytic activity for the degradation of AO7 and phenol. Moreover, the composites are demonstrated to be excellent photo-Fenton-like catalysts. The improved photocatalytic activity of the composites is mainly attributed to the efficient separation of photogenerated electrons and holes owing to the formation of the p-n heterojunction between $BiFeO_3$ and Ag_3PO_4.

Abbreviations

AO7: Acid orange 7; CB: Conduction band; DRS: UV-vis diffuse reflectance spectra; EDX: Energy dispersive X-ray; E_g: Bandgap energy; I-t: Photocurrent-time; NMP: 1-Methyl-2-pyrrolidione; PVDF: Polyvinylidene fluoride; R: Reflectance; SEM: Scanning electron microscope; TEM: Transmission electron microscope; VB: Valence band; XPS: X-ray photoelectron spectroscopy; XRD: X-ray diffractometer

Acknowledgements

The authors appreciate the National Natural Science Foundation of China (Grant No. 51662027, 51602170), the Natural Science Foundation of Qinghai, China (Grant No.2016-ZJ-954Q), and Chun Hui Program of Ministry of Education of China (Grant No. Z2016074, Z2016075).

Funding

This work was supported by the National Natural Science Foundation of China (Grant No. 51662027, 51602170), the Natural Science Foundation of Qinghai, China (Grant No.2016-ZJ-954Q), and Chun Hui Program of Ministry of Education of China (Grant No. Z2016074, Z2016075).

Availability of Data and Materials

All data analyzed during this investigation are presented in this article.

Authors' Contributions

HY and LD conceived the idea of experiments. LD and TX carried out the experiments. LD, HY, TX, and XC participated in the discussion and analysis of the experimental result. LD wrote the manuscript. HY and XC improved the manuscript. All authors read and approved the final manuscript.

Authors' Information

HY is a professor and a Ph.D. degree holder specializing in the investigation of photocatalytic and nanometer materials. XC is a professor and a Ph.D. degree holder specializing in the investigation of functional materials. LD is a doctoral candidate major in the preparation of photocatalytic materials. TX is a Ph.D. degree holder major in the investigation of photocatalytic materials.

Competing Interests

The authors declare that they have no competing interests and the mentioned received funding in our manuscript does not lead to any conflict of interests regarding the publication of this work.

Publisher's Note

Author details

[1]State Key Laboratory of Advanced Processing and Recycling of Non-ferrous Metals, Lanzhou University of Technology, Lanzhou 730050, China. [2]College of Physics and Electronic Information Engineering, Qinghai Normal University, Xining 810008, China.

Received: 30 May 2018 Accepted: 17 August 2018
Published online: 29 August 2018

References

1. Fujishima A, Zhang X, Tryk DA (2007) Heterogeneous photocatalysis: from water photolysis to applications in environmental cleanup. Int J Hydrog Energy 32:2664–2672
2. Wang ZL, Zhang JF, Lv JL, Dai K, Liang CH (2017) Plasmonic Ag_2MoO_4/AgBr/Ag composite: excellent photocatalytic performance and possible photocatalytic mechanism. Appl Surf Sci 396:791–798
3. Yan Y, Yang H, Zhao X, Li R, Wang X (2018) Enhanced photocatalytic activity of surface disorder-engineered $CaTiO_3$. Mater Res Bull 105:286–290
4. Lv JL, Liu J, Zhang JF, Dai K, Liang CH, Wang ZL, Zhu GP (2018) Construction of organic-inorganic cadmium sulfide/diethylenetriamine hybrids for efficient photocatalytic hydrogen production. J Colloid Interface Sci 512:77–85
5. Wang F, Yang H, Zhang YC (2018) Enhanced photocatalytic performance of $CuBi_2O_4$ particles decorated with Ag nanowires. Mater Sci Semicond Process 73:58–66
6. Lv JL, Zhang JF, Dai K, Liang CH, Zhu GP, Wang ZL, Li Z (2017) Controllable synthesis of inorganic-organic $Zn_{1-x}Cd_xS$-DETA solid solution nanoflowers and their enhanced visible-light photocatalytic hydrogen-production performance. Dalton Trans 46:11335–11343
7. Kokane SB, Sasikala R, Phase DM, Sartale SD (2017) In_2S_3 nanoparticles dispersed on g-C_3N_4 nanosheets: role of heterojunctions in photoinduced charge transfer and photoelectrochemical and photocatalytic performance. J Mater Sci 52:7077–7090
8. Li Z, Zhang JF, Lv JL, Lu LH, Liang CH, Dai K (2018) Sustainable synthesis of CeO_2/CdS-diethylenetriamine composites for enhanced photocatalytic hydrogen evolution under visible light. J Alloys Compd 758:162–170
9. Lv JL, Dai K, Zhang JF, Lu LH, Liang CH, Geng L, Wang ZL, Yuan GY, Zhu GP (2017) In situ controllable synthesis of novel surface plasmon resonance-enhanced Ag_2WO_4/Ag/Bi_2MoO_6 composite for enhanced and stable visible light photocatalyst. Appl Surf Sci 391:507–515
10. Ye Y, Yang H, Li R, Wang X (2017) Enhanced photocatalytic performance and mechanism of Ag-decorated $LaFeO_3$ nanoparticles. J Sol-Gel Sci Technol 82:509–518
11. Lv J, Dai K, Zhang J, Liu Q, Liang C, Zhu G (2017) Facile constructing novel 2D porous g-C_3N_4/BiOBr hybrid with enhanced visible-light-driven photocatalytic activity. Sep Purif Technol 178:6–17
12. Li J, Yin Y, Liu E, Ma Y, Wan J, Fan J, Hu X (2017) In situ growing Bi_2MoO_6 on g-C_3N_4 nanosheets with enhanced photocatalytic hydrogen evolution and disinfection of bacteria under visible light irradiation. J Hazard Mater 321:183–192
13. Wang ZL, Lv JL, Zhang JF, Dai K, Liang CH (2018) Facile synthesis of Z-scheme $BiVO_4$/porous graphite carbon nitride heterojunction for enhanced visible-light-driven photocatalyst. Appl Surf Sci 430:595–602
14. Xie T, Li H, Liu C, Xu L (2018) Facile synthesis of magnetic photocatalyst ag/$BiVO_4$/$Mn_{1-x}Zn_xFe_2O_4$ and its highly visible-light-driven photocatalytic activity. Materials 11:810
15. Deebasree JP, Maheskumar V, Vidhya B (2018) Investigation of the visible light photocatalytic activity of $BiVO_4$ prepared by sol gel method assisted by ultrasonication. Ultrason Sonochem 45:123–132
16. Hu TP, YangY DK, Zhang JF, Liang CH (2018) A novel Z-scheme Bi_2MoO_6/BiOBr photocatalyst for enhanced photocatalytic activity under visible light irradiation. Appl Surf Sci 456:473–481
17. Demirci S, Yurddaskal M, Dikici T, Sarıoğlu C (2018) Fabrication and characterization of novel iodine doped hollow and mesoporous hematite (Fe_2O_3) particles derived from sol-gel method and their photocatalytic performances. J Hazard Mater 345:27–37
18. Lv JL, Zhang JF, Liu J, Li Z, Dai K, Liang CH (2018) Bi SPR-promoted Z-scheme Bi_2MoO_6/CdS-diethylenetriamine composite with effectively enhanced visible light photocatalytic hydrogen evolution activity and stability. ACS Sustain Chem Eng 6:696–706
19. Zhao XX, Yang H, Li SH, Cui ZM, Zhang CR (2018) Synthesis and theoretical study of large-sized $Bi_4Ti_3O_{12}$ square nanosheets with high photocatalytic activity. Mater Res Bull 107:180–188
20. Gao F, Chen XY, Yin KB, Dong S, Ren ZF, Yuan F, YU T, Zou ZG, Liu JM (2007) Visible-light photocatalytic properties of weak magnetic $BiFeO_3$ nanoparticles. Adv Mater 19:2889–2892
21. Bai XF, Wei J, Tian BB, Liu Y, Reiss T, Guiblin N, Gemeiner P, Dkhil B, Infante IC (2016) Size effect on optical and photocatalytic properties in $BiFeO_3$ nanoparticles. J Phys Chem C 120:3595–3601
22. Ji W, Yao K, Lim YF, Liang YC, Suwardi A (2013) Epitaxial ferroelectric $BiFeO_3$ thin films for unassisted photocatalytic water splitting. Appl Phys Lett 103:062901
23. Pattnaik SP, Behera A, Martha S, Acharya R, Parida K (2018) Synthesis, photoelectrochemical properties and solar light-induced photocatalytic activity of bismuth ferrite nanoparticles. J Nanopart Res 20:10

24. Lam SM, Sin JC, Mohamed AR (2017) A newly emerging visible light-responsive $BiFeO_3$ perovskite for photocatalytic applications: a mini review. Mater Res Bull 90:15–30
25. Di LJ, Yang H, Xian T, Chen XJ (2017) Enhanced photocatalytic activity of $NaBH_4$ reduced $BiFeO_3$ nanoparticles for rhodamine B decolorization. Materials 10:1118
26. Tseng WJ, Lin RD (2014) $BiFeO_3$/a-Fe_2O_3 core/shell composite particles for fast and selective removal of methyl orange dye in water. J Colloid Interface Sci 428:95–100
27. Zhang T, Shen Y, Qiu YH, Liu Y, Xiong R, Shi J, Wei JH (2017) Facial synthesis and photoreaction mechanism of $BiFeO_3$/$Bi_2Fe_4O_9$ heterojunction nanofibers. ACS Sustain Chem Eng 5:4630–4636
28. Li HF, Quan X, Chen S, Yu HT (2017) Ferroelectric-enhanced Z-schematic electron transfer in $BiVO_4$-$BiFeO_3$-$CuInS_2$ for efficient photocatalytic pollutant degradation. Appl Catal B Environ 209:591–599
29. Chaiwichian S, Wetchakun K, Kangwansupamonkon W, Wetchakun N (2017) Novel visible-light-driven $BiFeO_3$-Bi_2WO_6 nanocomposites toward degradation of dyes. J Photochem Photobiol A Chem 349:183–192
30. Wang L, Niu CG, Wang Y, Wang Y, Zeng GM (2016) The synthesis of Ag/AgCl/$BiFeO_3$ photocatalyst with enhanced visible photocatalytic activity. Ceram Int 42:18605–18611
31. Di LJ, Yang H, Xian T, Chen XJ (2018) Enhanced photocatalytic degradation activity of $BiFeO_3$ microspheres by decoration with g-C_3N_4 nanoparticles. Mater Res 21:e20180081
32. Yi Z, Ye J, Kikugawa N, Kako T, Ouyang SX, Stuart-Williams H, Yang H, Cao JY, Luo WJ, Li ZS, Liu Y, Withers RL (2010) An orthophosphate semiconductor with photooxidation properties under visible-light irradiation. Nat Mater 9:559–564
33. Bi YP, Ouyang SX, Umezawa N, Cao JY, Ye JH (2011) Facet effect of single-crystalline Ag_3PO_4 sub-microcrystals on photocatalytic properties. J Am Chem Soc 133:6490–6492
34. Amornpitoksuk P, Intarasuwan K, Suwanboon S, Baltrusaitis J (2013) Effect of phosphate salts (Na_3PO_4,Na_2HPO_4, and NaH_2PO_4) on Ag_3PO_4 morphology for photocatalytic dye degradation under visible light and toxicity of the degraded dye products. Ind Eng Chem Res 52:17369–17375
35. Reheman A, Tursun Y, Dilinuer T, Halidan M, Kadeer K, Abulizi A (2018) Facile one-step sonochemical synthesis and photocatalytic properties of graphene/Ag_3PO_4 quantum dots composites. Nanoscale Res Lett 13:70
36. Wang LP, Wang LM, Chu DQ, Wang ZF, Zhang YF, Sun JJ (2017) Tartaric acid-assisted synthesis of Ag_3PO_4 hollow microspheres with enhanced photocatalytic properties. Catal Commun 88:53–55
37. Hsieh MS, Su HJ, Hsieh PL, Chiang YW, Huang MH (2017) Synthesis of Ag_3PO_4 crystals with tunable shapes for facet-dependent optical property, photocatalytic activity, and electrical conductivity examinations. ACS Appl Mater Interfaces 9:39086–39093
38. Zheng C, Yang H (2018) Assembly of Ag_3PO_4 nanoparticles on rose flower-like Bi_2WO_6 hierarchical architectures for achieving high photocatalytic performance. J Mater Sci Mater Electron 29:9291–9300
39. Mohaghegh N, Rahimi E, Gholami MR (2015) Ag_3PO_4/$BiPO_4$ p-n heterojunction nanocomposite prepared in room-temperature ionic liquid medium with improved photocatalytic activity. Mater Sci Semicond Process 39:506–514
40. Hu Y, Dong C, Wu KL (2015) Synthesis of Ag_3PO_4-$Bi_2O_2CO_3$ composites with high visible-light photocatalytic activity. Mater Lett 147:69–71
41. Xu H, Zhao HZ, Song YH, Yan W, Xu YG, Li HP, Huang LY, Yin S, Li YP, Zhang Q, Li HM (2015) g-C_3N_4/Ag_3PO_4 composites with synergistic effect for increased photocatalytic activity under the visible light irradiation. Mater Sci Semicond Process 39:726–734
42. Qi XM, Gu ML, Zhu XY, Wu J, Wu Q, Long HM, He K (2016) Controlled synthesis of Ag_3PO_4/$BiVO_4$ composites with enhanced visible-light photocatalytic performance for the degradation of RhB and 2,4-DCP. Mater Res Bull 80:215–222
43. Zheng CX, Yang H, Cui ZM, Wang XX (2017) A novel $Bi_4Ti_3O_{12}$/Ag_3PO_4 heterojunction photocatalyst with enhanced photocatalytic performance. Nanoscale Res Lett 12:608
44. Hou GQ, Li YK, An WJ, Gao SJ, Zhang WL, Cui WQ (2017) Fabrication and photocatalytic activity of floating type Ag_3PO_4/$ZnFe_2O_4$/FACs photocatalyst. Mater Res Bull 94:263–271
45. Lu JS, Wang YJ, Liu F, Zhang L, Chai S (2017) Fabrication of a direct Z-scheme type WO_3/Ag_3PO_4 composite photocatalyst with enhanced visible-light photocatalytic performances. Appl Surf Sci 393:180–190
46. Li QS, Yang C (2017) Facile fabrication of Ag_3PO_4 supported on ZnO inverse opals for enhancement of solar-driven photocatalysis. Mater Lett 199:168–171
47. Wang ZL, Lv JL, Dai K, Lu LH, Liang CH, Geng L (2016) Large scale and facile synthesis of novel Z-scheme Bi_2MoO_6/Ag_3PO_4 composite for enhanced visible light photocatalyst. Mater Lett 169:250–253
48. Dong W, Gou YP, Guo B, Li H, Liu HZ, Joel TW (2013) Enhanced photovoltaic effect in $BiVO_4$ semiconductor by incorporation with an ultrathin $BiFeO_3$ ferroelectric layer. ACS Appl Mater Interfaces 5:6925–6929
49. Wang F, Yang H, Zhang H, Jiang J (2018) Growth process and enhanced photocatalytic performance of $CuBi_2O_4$ hierarchical microcuboids decorated with AuAg alloy nanoparticles. J Mater Sci Mater Electron 29:1304–1316
50. Zhao X, Yang H, Cui Z, Li R, Feng W (2017) Enhanced photocatalytic performance of Ag-$Bi_4Ti_3O_{12}$ nanocomposites prepared by a photocatalytic reduction method. Mater Technol 32:870–880
51. Tan P, Chen X, Wu L, Shang YY, Liu W, Pan J, Xiong X (2017) Hierarchical flower-like $SnSe_2$ supported Ag_3PO_4 nanoparticles: towards visible light driven photocatalyst with enhanced performance. Appl Catal B Environ 202:326–334
52. Zhao WH, Wei ZQ, Zhu XL, Zhang XD, Jiang JL (2018) Optical and magnetic properties of diluted magnetic semiconductors $Zn_{0.95}M_{0.05}S$ nanorods prepared by hydrothermal method. Int J Mater Res 109:405–412
53. Yan Y, Yang H, Zhao X, Zhang H, Jiang J (2018) A hydrothermal route to the synthesis of $CaTiO_3$ nanocuboids using P25 as the titanium source. J Electron Mater 47:3045–3050
54. Jia YF, Wu CJ, Kim DH, Lee BW, Rhee SJ, Park YC, Kim CS, Wang QJ, Liu C (2018) Nitrogen doped $BiFeO_3$ with enhanced magnetic properties and photo-Fenton catalytic activity for degradation of bisphenol A under visible light. Chem Eng J 337:709–721
55. Soltani T, Lee BK (2016) Novel and facile synthesis of Ba-doped $BiFeO_3$ nanoparticles and enhancement of their magnetic and photocatalytic activities for complete degradation of benzene in aqueous solution. J Hazard Mater 316:122–133
56. An JJ, Zhu LH, Wang N, Song Z, Yang ZY, Du DY, Tang HQ (2013) Photo-Fenton like degradation of tetrabromobisphenol A with graphene-$BiFeO_3$ composite as a catalyst. Chem Eng J 219:225–237
57. Ye Y, Yang H, Wang X, Feng W (2018) Photocatalytic, Fenton and photo-Fenton degradation of RhB over Z-scheme g-C_3N_4/$LaFeO_3$ heterojunction photocatalysts. Mater Sci Semicond Process 82:14–24
58. Morrison SR (1980) Electrochemistry at semiconductor and oxidized metal electrode. Plenum, NewYork
59. Cui ZM, Yang H, Zhao XX (2018) Enhanced photocatalytic performance of g-C_3N_4/$Bi_4Ti_3O_{12}$ heterojunction. Mater Sci Eng B 229:160–172
60. Andersen T, Haugen HK, Hotop H (1999) Binding energies in atomic negative ions: III. J Phys Chem Ref Data 28:1511–1533